

References and Notes

1. C. A. Angell, K. L. Ngai, G. B. McKenna, P. F. McMillan, S. W. Martin, *J. Appl. Phys.* **88**, 3113 (2000).
2. M. D. Ediger, *Annu. Rev. Phys. Chem.* **51**, 99 (2000).
3. H. Sillescu, *J. Non-Cryst. Solids* **243**, 81 (1999).
4. M. D. Ediger, C. A. Angell, S. R. Nagel, *J. Phys. Chem.* **100**, 13200 (1996).
5. J. T. Fourkas, D. Kivelson, U. Mohanty, K. A. Nelson, Eds., *Supercooled Liquids: Advances and Novel Applications*, vol. 676 of *ACS Symposium Series* (American Chemical Society, Washington, DC, 1997).
6. G. Harrison, *The Dynamic Properties of Supercooled Liquids* (Academic Press, New York, 1976).
7. T. Gleim, W. Kob, K. Binder, *Phys. Rev. Lett.* **81**, 4404 (1998).
8. D. B. Hall, A. Dhinojwala, J. M. Torkelson, *Phys. Rev. Lett.* **79**, 103 (1997).
9. G. Adam, J. H. Gibbs, *J. Chem. Phys.* **43**, 139 (1965).
10. H. Wendt, R. Richert, *Phys. Rev. E* **61**, 1722 (2000).
11. E. R. Weeks, J. C. Crocker, A. C. Levitt, A. Schofield, D. A. Weitz, *Science* **287**, 627 (2000).
12. C.-Y. Wang, M. D. Ediger, *J. Phys. Chem. B* **104**, 1724 (2000).
13. I. Chang, H. Sillescu, *J. Phys. Chem. B* **101**, 8794 (1997).
14. K. L. Ngai, *J. Phys. Chem. B* **103**, 10684 (1999).
15. R. Richert, *J. Phys. Chem. B* **101**, 6323 (1997).
16. E. V. Russell, N. E. Israeloff, *Nature* **408**, 695 (2000).
17. W. E. Moerner, *Science* **265**, 46 (1994).
18. P. F. Barbara, W. E. Moerner, *Acc. Chem. Res.* **29**, 561 (1996).
19. H. P. Lu, X. S. Xie, *Nature* **385**, 143 (1997).
20. S. Nie, D. T. Chiu, R. N. Zare, *Science* **266**, 1018 (1994).
21. D. A. Vanden Bout *et al.*, *Science* **277**, 1074 (1997).
22. R. M. Dickson, A. B. Cubitt, R. Y. Tsien, W. E. Moerner, *Nature* **388**, 355 (1997).
23. T. Basche, S. Kummer, C. Braeuchle, *Nature* **373**, 132 (1995).
24. The single-molecule environment is probe dependent, with its size determined by the dye used.
25. J. J. Macklin, J. K. Trautman, T. D. Harris, L. E. Brus, *Science* **272**, 255 (1996).
26. The sample is held atop a closed loop piezo scanning stage and illuminated with the second harmonic of a Nd:yttrium-aluminum-garnet laser through a 1.25 numerical aperture (NA) oil immersion objective in the epi configuration. By scanning the sample in the focus of a laser beam, we can observe the fluorescence from individual molecules. The fluorescence signal from the molecules is passed through a dichroic beam splitter to remove excitation light and split into two orthogonal polarizations, which are imaged onto the front of two single-photon-counting avalanche photodiodes. For temperature-dependent data, the sample was held at constant temperature in an Oxford Microstat-N cryostat, and the fluorescence was excited and collected through a 0.6-NA long working distance air objective. All other aspects of the experiment remain unchanged.
27. The T_g of the polymer was measured by differential scanning calorimetry.
28. T. Ha, T. A. Laurence, D. S. Chemla, S. Weiss, *J. Phys. Chem. B* **103**, 6839 (1999).
29. R. M. Dickson, A. P. Bartko, *J. Phys. Chem. B* **103**, 3053 (1999).
30. R. M. Dickson, D. J. Norris, Y.-L. Tzeng, W. E. Moerner, *Science* **274**, 966 (1996).
31. Measurement of the full three-dimensional orientation (27, 28) is not required because the dynamics are isotropic in three dimensions and thus revealed fully in the fluctuations of the dichroism. Additionally, the use of a high NA objective (NA = 1.25) leads to a slight contamination of the dichroism signal due to the out-of-plane component of the fluorescence that manifests itself as an additional background but does not adversely affect the measured dynamics (28).
32. J. A. Veerman, M. F. Garcia-Parajo, L. Kuipers, N. F. van Hulst, *Phys. Rev. Lett.* **83**, 2155 (1999).
33. T. Ha, J. Glass, T. Enderle, D. S. Chemla, S. Weiss, *Phys. Rev. Lett.* **80**, 2093 (1998).
34. G. E. P. Box, G. M. Jenkins, *Time Series Analysis Forecasting and Control* (Holden-Day, San Francisco, 1976).
35. For all correlation functions, the first point containing the noise is not shown and not included in the fit. Fits

of correlation functions yield coefficient of determination R^2 values greater than 0.99 in most cases. Standard errors for the fitting parameters tend to be extremely small (1 part in 10^5) but provide little meaningful basis for comparison because of the large covariance of β and τ . A useful measure of this error determines that a 1% variation in β or a 5% variation in τ is sufficient to reduce the R^2 value from 0.99 to 0.98. The rotational correlation time τ_c is defined as the integral from zero to infinity of the correlation function, but for a stretched exponential function, this integral can be conveniently written in terms of the τ and β parameters as

$$\tau_c = \int_0^\infty C(t) dt = \frac{\tau_{\text{KWW}}}{\beta_{\text{KWW}}} \Gamma\left(\frac{1}{\beta_{\text{KWW}}}\right)$$

where Γ is the gamma function, defined as $\Gamma(n) = \int_0^\infty e^{-x} x^{n-1} dx$.

36. The orientational transient can be calculated from the polarized fluorescence data with

$$\theta(t) = \tan^{-1} \left[\sqrt{\frac{I(t)}{I_\perp(t)}} \right]$$

Molecules were determined to have exchanged environments when the average angle jump changes by more than 2 SD from the previous average angle jump.

37. C. Bennemann, C. Donati, J. Baschnagel, S. C. Glotzer, *Nature* **399**, 246 (1999).

38. D.A.V.B. is a Research Corporation Cottrell Scholar and a Camille and Henry Dreyfus Foundation New Faculty Awardee. This work is supported by grants from the Research Corporation.

10 October 2000; accepted 28 February 2001

Real-Space Imaging of Nucleation and Growth in Colloidal Crystallization

U. Gasser,^{1*} Eric R. Weeks,^{1†} Andrew Schofield,² P. N. Pusey,² D. A. Weitz¹

Crystallization of concentrated colloidal suspensions was studied in real space with laser scanning confocal microscopy. Direct imaging in three dimensions allowed identification and observation of both nucleation and growth of crystalline regions, providing an experimental measure of properties of the nucleating crystallites. By following their evolution, we identified critical nuclei, determined nucleation rates, and measured the average surface tension of the crystal-liquid interface. The structure of the nuclei was the same as the bulk solid phase, random hexagonal close-packed, and their average shape was rather nonspherical, with rough rather than faceted surfaces.

The study of the structure, growth, and properties of crystals is one of the most important areas of solid state physics (*1*). Although a great deal is known about the behavior of bulk crystals, considerably less is known about their earliest stage, when they nucleate and grow from a liquid. Homogeneous nucleation occurs when small crystalline regions form from structural fluctuations in a liquid cooled below its freezing point. The growth of these regions depends on a competition between a decrease in bulk energy, which favors growth, and an increase in surface energy, which favors shrinkage. The smallest crystals continually form by fluctuations but then typically shrink away because of the high surface energy. Growth becomes energetically favorable only when the crystallites reach a critical size. The competition between

the surface energy and bulk energy is reflected in the free energy for a spherical crystallite

$$\Delta G = 4\pi r^2 \gamma - \frac{4\pi}{3} r^3 \Delta\mu n \quad (1)$$

where r is the radius, γ is the free energy of the crystal-liquid interface per unit area, $\Delta\mu$ is the difference between the liquid and solid chemical potentials, and n is the number density of particles in the crystallite (*2*). The size of the critical nucleus is $r_c = 2\gamma/(\Delta\mu n)$, corresponding to the maximum of ΔG (Eq. 1). Despite its crucial role, very little is known about this nucleation process, primarily because of the difficulty of directly observing the nuclei in real space.

No experiment has ever directly measured the size of the critical nucleus. It cannot be determined theoretically—even the surface tension is unknown. Furthermore, an additional important yet unresolved question involves the internal structure of critical nuclei, because nucleation need not occur via the stable bulk phase (*3*). General arguments based on symmetry suggest that nucleation may proceed by a body-centered cubic (bcc) structure as an intermediate phase, with the final equilibrium solid phase having a differ-

¹Department of Physics and Division of Engineering and Applied Sciences, Harvard University, Cambridge, MA 02138, USA. ²Department of Physics and Astronomy, University of Edinburgh, Edinburgh, Scotland EH9 3JZ, UK.

*To whom correspondence should be addressed. E-mail: gasser@deas.harvard.edu

†Present address: Physics Department, Emory University, Atlanta, GA 30322, USA.

REPORTS

ent symmetry (4). Computer simulations of a Lennard-Jones system found critical nuclei with a face-centered cubic (fcc) core and a predominantly bcc surface layer (5). However, light-scattering measurements from hard spheres (6–8), which provide an average over crystalline regions of all sizes, suggest that nucleation occurs through the random hexagonal close-packed (rhcp) phase, a random mixture of hexagonal close-packed (hcp) and fcc-like stackings of planes with hexagonal order, and this is supported by recent computer simulations (9). The important questions about the structure and size of the nucleating crystallites can best be resolved by direct experimental observation in real space.

The small length and time scales that characterize homogeneous crystal nucleation have to date precluded this direct real-space observation of critical nuclei in atomic or molecular systems. By contrast, however, colloidal systems can be studied directly, because their larger size and concomitant slower time scale makes them much more experimentally accessible. Colloidal particles can serve as good models for atomic or molecular materials; they show an analogous phase diagram (10), and the volume exclusion that results in crystallization of colloidal particles also plays a dominant role in traditional crystallization (2). Concentrated suspensions of hard-sphere colloids crystallize because of entropy (11): The free volume for ordered spheres (maximum packing volume fraction $\phi = 0.74$) is greater than that of disordered spheres (maximum packing $\phi \approx 0.64$), and thus, the entropy is higher in the crystalline state. The phase behavior is determined solely by the volume fraction ϕ , with freezing occurring at $\phi_f^{\text{HS}} = 0.494$ and melting occurring at $\phi_m^{\text{HS}} = 0.545$ (HS, hard sphere) (12). Weakly charged colloids behave in essentially the same

manner, but the boundaries of the phase diagram are shifted to slightly lower ϕ values (11). Colloidal (6–8, 13–16) and protein (17) systems have been valuable for studying crystal nucleation, but these studies did not directly visualize the critical nuclei and thus were unable to directly observe their properties.

We report on three-dimensional real-space imaging of the nucleation and growth of nearly hard-sphere colloidal crystals. We observed the formation of the smallest nuclei, which shrink far more frequently than they grow; by measuring their size distribution, we were able to directly determine the surface tension of a colloidal crystal. We were also able to determine the size of the critical nuclei by observing when the probability to grow exceeds the probability to shrink. We found that the structure of critical nuclei is rhcp, the same as that of the bulk. The critical nuclei have rough surfaces, and their average shape is ellipsoidal.

We used poly(methyl methacrylate) spheres sterically stabilized with poly-12-hydroxystearic acid (18, 19), with a radius $a = 1.26 \mu\text{m}$ and a polydispersity of $<5\%$. They were suspended in a mixture of decahydronaphthalene and cyclohexylbromide, which closely matches both the refractive index and the density of the particles. To make the particles visible with fluorescence microscopy, we dyed them with rhodamine, which gives the particles a small charge, resulting in freezing at $\phi_f = 0.38$ and melting at $\phi_m = 0.42$ (20). We used a fast laser scanning confocal microscope, which allowed us to measure the three-dimensional arrangement of colloidal particles in suspension (21, 22). We observed a $58 \mu\text{m}$ by $55 \mu\text{m}$ by $20 \mu\text{m}$ volume, containing ~ 4000 particles. The total volume of our samples was $\sim 50 \mu\text{l}$, and they contained a short piece of paramagnetic wire, which we agitated with a magnet to shear melt

the sample before observation. Heterogeneous nucleation at the walls of the sample chamber was suppressed by fusing colloidal particles of a smaller size onto the walls before adding the colloidal samples. Further, we focused at least 8 and typically 15 particle diameters from the walls to ensure that we studied bulk homogeneous nucleation.

We observed the growth of crystallites by extracting the particle centers from the raw images with an accuracy of $\sim 0.04 \mu\text{m}$ (23). From these particle positions, crystalline regions were identified with an algorithm that finds ordered regions, independent of any particular crystal structure (5, 24). It relies on the assumptions that the neighbors of a particle in a crystal lattice are arranged in a particular orientation about the particle and that this orientation of neighbors is the same for nearby particles. Quantitatively, this is achieved by calculating local bond-order parameters (25) that are based on spherical harmonics Y_{lm} and are a measure of the orientation of the neighbors around a particle. Two adjacent particles with similar orientation of

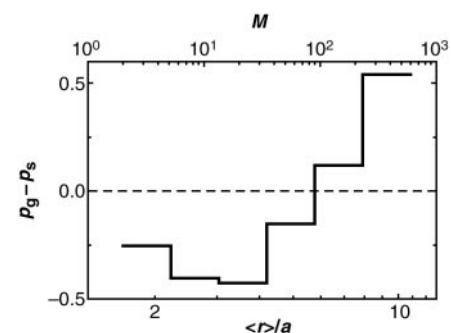


Fig. 2. The difference $p_g - p_s$ of the probabilities with which a crystallite is growing or shrinking plotted against the normalized average crystallite radius $\langle r \rangle/a$ (bottom) and the number of particles M in the crystallite (top) for $\phi = 0.47$. The size of the critical nucleus lies in the range in which $p_g - p_s$ goes from negative to positive values.

Fig. 1. Four snapshots during crystallization of a sample with $\phi = 0.45$. The red spheres are drawn to scale and represent particles that were identified as crystal-like. The particles in the metastable liquid state are shown by the blue spheres, reduced in size for clarity. (A) Time $t = 20$ min after shear melting, (B) $t = 43$ min, (C) $t = 66$ min, and (D) $t = 89$ min.

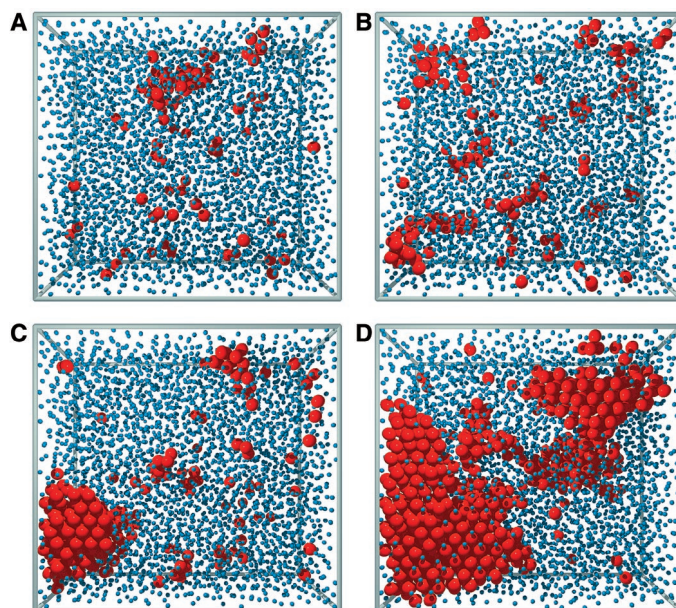


Table 1. The experimentally measured bond-order histograms for the crystal regions were least squares fit with the histograms for crystals and liquid. For three samples, the fraction of each structure type found by the fit is given, with the sum of all the fractions constrained to be 1. The values in parentheses are the uncertainty of the last digit. The sum of the squared differences between the measurement and the fit, Δ^2 , is a measure for the quality of the fit, with smaller values indicating a better fit. The fit for the $\phi = 0.45$ sample is shown in Fig. 4.

ϕ	Δ^2	bcc	fcc	hcp	Liquid
0.49	0.021	0.00(3)	0.10(3)	0.32(6)	0.58(14)
0.45	0.006	0.00(1)	0.58(7)	0.20(3)	0.22(6)
0.43	0.006	0.00(3)	0.34(5)	0.25(4)	0.41(10)

REPORTS

their neighbors have similar bond-order parameters and are therefore said to be joined by a crystal-like “bond” (26). Even in the disordered liquid, crystal-like bonds are not uncommon; thus, only particles with eight or more crystal-like bonds are defined as being crystal-like. All particles in a crystallite with perfect fcc, hcp, rhcp, or bcc structure are correctly recognized, whereas only an insignificant number of particles in the liquid are found to be crystal-like.

At the beginning of an experiment, samples started in the metastable liquid state, but because of random structural fluctuations, subcritical nuclei of crystal-like par-

ticles were present. This is shown in two early-time snapshots (Fig. 1, A and B), where we represent crystal-like particles as red spheres and liquid-like particles as blue spheres, shown with a reduced diameter to improve visibility. Typically, these subcritical nuclei contained no more than 20 particles and shrank to reduce their surface energy. After a strongly ϕ -dependent period of time, critical nuclei formed and rapidly grew into large postcritical crystallites (Fig. 1, C and D). By following the time evolution of many crystallites, we determined the size dependence of the probabilities p_g and p_s with which crystallites grow

or shrink (27). Because $p_g = p_s$ at the critical size, we plot the difference $p_g - p_s$ as a function of crystallite radius and particle number M in Fig. 2 for a sample with $\phi = 0.47$. We found an abrupt change from negative to positive values of $p_g - p_s$ (28), allowing us to identify the critical size, which is $60 < M < 160$, in good agreement with recent computer simulations (9). This corresponds to $r_c \approx 6.2a$, assuming a spherical nucleus. The volume fraction of the nuclei is larger than the ϕ value of the fluid; above coexistence, the difference is $\Delta\phi = 0.012 \pm 0.003$, independent of ϕ , where $\Delta\phi$ increases slightly for $M > 100$. We can understand this $\Delta\phi$ value as resulting from the higher osmotic pressure exerted by the fluid on the nuclei (16), whereas in the coexistence regime, $\Delta\phi$ must reflect the evolution of ϕ to the higher value, ultimately attained by the crystallites, where $\Delta\phi = \phi_m - \phi_f$. The nucleation rate densities were slower than $5 \text{ mm}^{-3} \text{ s}^{-1}$ for $\phi < 0.45$, as well as for $\phi > 0.53$. Values of the order of $10 \text{ mm}^{-3} \text{ s}^{-1}$ were found for $0.45 < \phi < 0.53$. However, for $0.47 < \phi < 0.53$, the average size of the nuclei began to grow immediately after shear melting; thus, there was little time for the sample to equilibrate after shear melting, and we were not able to observe the formation process of critical nuclei entirely. Our nucleation rate densities are of the same magnitude as values obtained by small-angle light scattering from hard spheres (29, 30) but are two orders of magnitude larger than those obtained from Bragg scattering (31).

The direct imaging afforded by confocal microscopy enabled us to determine the structure and shape of individual nuclei. In Fig. 3, A through C, we show a crystallite that is slightly larger than the critical size. Again, the red spheres represent crystal-like particles, and the blue ones depict particles in the liquid state that are on the

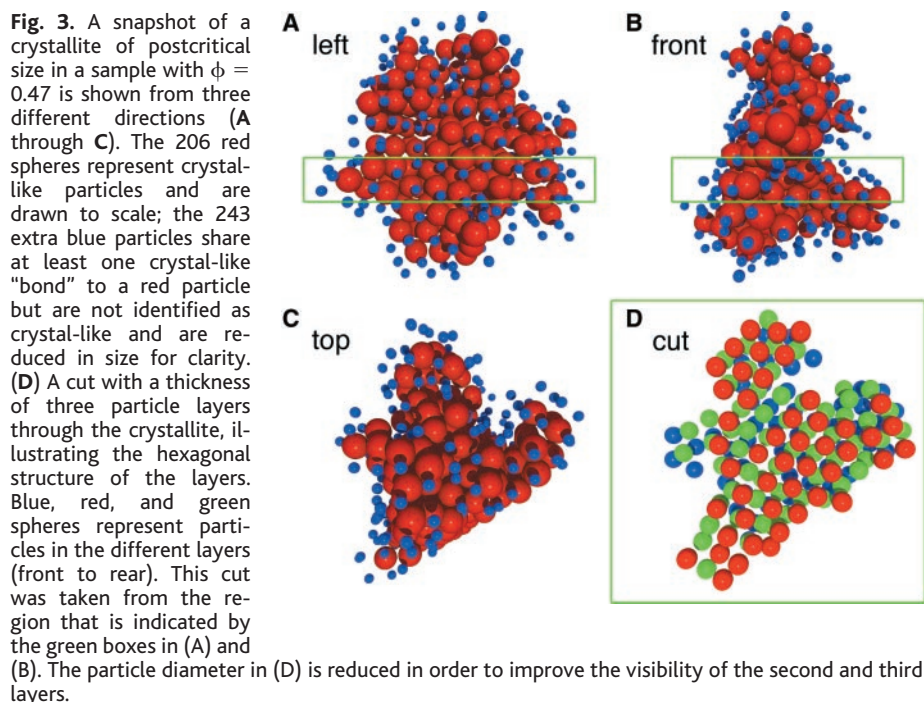


Fig. 3. A snapshot of a postcritical crystallite in a sample with $\phi = 0.47$ is shown from three different directions (A through C). The 206 red spheres represent crystal-like particles and are drawn to scale; the 243 extra blue particles share at least one crystal-like “bond” to a red particle but are not identified as crystal-like and are reduced in size for clarity. (D) A cut with a thickness of three particle layers through the crystallite, illustrating the hexagonal structure of the layers. Blue, red, and green spheres represent particles in the different layers (front to rear). This cut was taken from the region that is indicated by the green boxes in (A) and (B). The particle diameter in (D) is reduced in order to improve the visibility of the second and third layers.

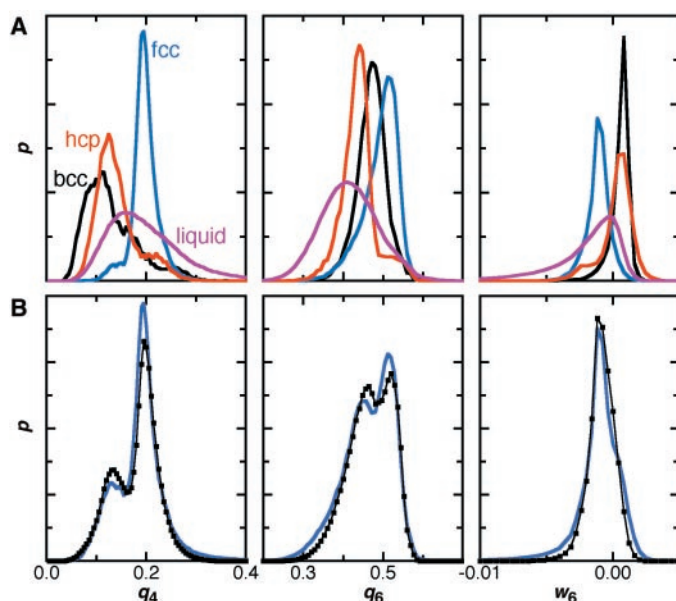


Fig. 4. (A) q_4 , q_6 , and w_6 bond-order parameter histograms for fcc (blue curves), hcp (red curves), bcc (black curves), and liquid (purple curves). (B) The measured bond-order histograms (black plots) of a sample with $\phi = 0.45$ are shown together with a least squares fit (blue curve) using the bond-order histograms from (A). The results of this and other structure fits are summarized in Table 1.

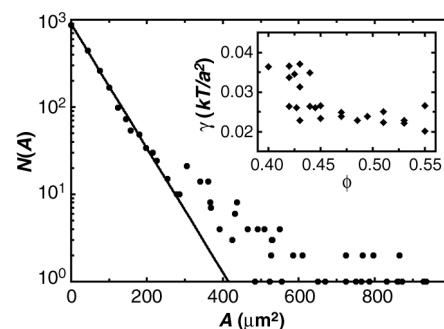


Fig. 5. The number of nuclei $N(A)$ (circles) is shown as a function of the nucleus surface area A approximated by an ellipsoid ($\phi = 0.445$). From the fit (line) with the function $N(A) = \text{constant} \cdot \exp[-A\gamma/(k_B T)]$, the surface tension $\gamma = 0.026k_B T/a^2$ is determined. The values of γ for all samples are given in the inset as a function of ϕ .

surface of the crystallite and have at least one crystal-like bond with a red particle. The cores of the crystalline nuclei are formed from hexagonal layers, as shown by the cut through the center of this crystallite (Fig. 3D), and their surfaces are more disordered. The interface between the highly ordered cores and the amorphous liquid exterior is not sharp; this decrease in order from the interior to the exterior is in agreement with computer simulations of a Lennard-Jones system (5) and density functional calculations for hard spheres (32).

To determine the crystal structure of the ordered cores, we used the rotational invariants $q_4(i)$, $q_6(i)$, and $w_6(i)$ (33), which are quantitative measures for the local order around particle i , and distinguished between fcc, hcp, bcc, and liquid (5, 9, 24). Because of thermal fluctuations, even homogeneous crystals have a distribution of these parameters. Nevertheless, these distributions are distinct for every crystal structure, as shown by the calculations (34) in Fig. 4A. These are compared to measurements of experimental crystalline nuclei, shown by a black curve in Fig. 4B. The blue curve is a least squares fit with the distributions from Fig. 4A, and the fit parameters are summarized in Table 1. During the nucleation process, bcc order is completely absent; in particular, as shown in Fig. 4, the q_4 distribution for bcc is markedly different from the measured distribution. Instead, the main contributions to the structure of the experimental crystalline nuclei are due to fcc, hcp, and liquid. The mixture of fcc and hcp is the signature of rhcp structure and is consistent with the stacked hexagonal planes in Fig. 3D. The liquid contribution in the fit is mainly due to the surface of the crystallites. These results are in agreement with those expected for hard spheres, which also crystallize in the rhcp structure (7), confirming that the critical nuclei are formed only from the bulk solid phase, rather than forming from a different metastable solid phase.

In classical nucleation theory (2), it is assumed that the nuclei have a spherical shape due to surface tension. To the best of our knowledge, this assumption has never been experimentally verified. As shown by the example in Fig. 3, our data indicate that the crystallite surfaces were quite rough, suggesting that the surface tension is low. Consistent with this, the crystallite shapes appeared rather nonspherical. To confirm this, we approximated each nucleus with an ellipsoid and found that the average nucleus is best described by an ellipsoid whose major axes have the ratio 1:1.8:3.2. Nuclei containing >50 particles were found to be somewhat less anisotropic than smaller ones, but on average, the ratio of the shortest and longest

ellipsoid axes was never higher than 0.65 ± 0.15 for nuclei of all sizes. This suggests that the effects of the nonspherical shape could be included in any future modification of the theory. Furthermore, we found that the radius of gyration r_g of crystallites was related to the number of particles M within each crystallite as $M(r_g) \propto r_g^{d_f}$ with the fractal dimension $d_f = 2.35 \pm 0.15$ for all values of ϕ ; the fractal behavior presumably reflects the roughness of their surfaces.

The interfacial tension between the crystal and fluid phases is a key parameter that controls the nucleation process, yet γ is difficult to calculate (1, 2) and to measure experimentally, but with our data, we can directly measure γ by examining the statistics of the smallest nuclei. For $r \ll r_c$, the surface term in Eq. 1 dominates the free energy of the crystallites, and consequently, we expect the number of crystallites to be $N(A) \propto \exp[-A\gamma/(k_B T)]$, where A is the surface area, which we approximate by an ellipsoid. In Fig. 5, we show that this proportionality does indeed hold, allowing us to obtain values for the surface tension. As shown in the inset, $\gamma \approx 0.027k_B T/a^2$ and may decrease slightly with increasing ϕ values. This value of γ is in reasonable agreement with density functional calculations for hard spheres and Lennard-Jones systems (32). By contrast, an older density functional study (35) and computer simulations of hard spheres (9, 36) gave results approximately four times as large. Our measurement of a low value of γ is consistent with the observed rough surfaces of the crystallites; this may reflect the effects of the softer potential due to the weak charges of our particles. Approximating the critical nucleus as an ellipsoid, with $M_c \approx 110$, we obtain $A_c = 880 \mu\text{m}^2$, $\Delta\mu \approx 0.13k_B T$, and $\Delta G(A_c) \approx 7.4k_B T$.

The direct observation of the structure, dynamics, and evolution of small crystalline nuclei allowed us to characterize the key processes of nucleation and growth of colloidal crystals and to quantitatively determine the important parameters that control this process. These results also provide crucial experimental input to help guide any future refinements of theories for nucleation and growth of colloidal crystals. Moreover, the ability to obtain three-dimensional movies of the dynamics of colloidal solids will allow the direct observation and study of other important phenomena, such as defect motion, effects of impurities, and crystallization of colloidal alloys.

References and Notes

1. T. Palberg, *J. Phys. Condens. Matter* **11**, R323 (1999).
2. K. F. Kelton, in *Solid State Physics*, H. Ehrenbach, D. Turnbull, Eds. (Academic Press, Boston, 1991), vol. 45, pp. 75–177.
3. W. Ostwald, *Z. Phys. Chem.* **22**, 289 (1897).

4. S. Alexander, J. P. McTague, *Phys. Rev. Lett.* **41**, 702 (1978).
5. P. R. ten Wolde, M. J. Ruiz-Montero, D. Frenkel, *J. Chem. Phys.* **104**, 9932 (1996).
6. P. N. Pusey, W. van Meegen, *Nature* **320**, 340 (1986).
7. P. N. Pusey et al., *Phys. Rev. Lett.* **63**, 2753 (1989).
8. J. Zhu et al., *Nature* **387**, 883 (1997).
9. S. Auer, D. Frenkel, *Nature* **409**, 1020 (2001).
10. P. N. Pusey, in *Liquids, Freezing and the Glass Transition*, D. Levesque, J. P. Hansen, J. Zinn-Justin, Eds. (Elsevier, Amsterdam, 1991), pp. 763–942.
11. A. K. Sood, in *Solid State Physics*, H. Ehrenbach, D. Turnbull, Eds. (Academic Press, Boston, 1991), vol. 45, pp. 1–73.
12. B. J. Alder, W. G. Hoover, D. A. Young, *J. Chem. Phys.* **49**, 3688 (1968).
13. K. Schätzel, B. J. Ackerson, *Phys. Rev. Lett.* **68**, 337 (1992).
14. P. Bartlett, R. H. Ottewill, P. N. Pusey, *Phys. Rev. Lett.* **68**, 3801 (1992).
15. Y. He, B. J. Ackerson, W. van Meegen, S. M. Underwood, K. Schätzel, *Phys. Rev. E* **54**, 5286 (1996).
16. B. J. Ackerson, K. Schätzel, *Phys. Rev. E* **52**, 6448 (1995).
17. S.-T. Yau, P. G. Vekilov, *Nature* **406**, 494 (2000).
18. L. Antl et al., *Colloids Surf.* **17**, 67 (1986).
19. S.-E. Phan et al., *Phys. Rev. E* **54**, 6633 (1996).
20. We determined the particle radius by measuring the volume per particle at random close packing ($\phi_{rcp} = 0.64$) and rhcp ($\phi_{rhcp} = 0.74$) with the microscope. We obtained the same particle radius from these two points in phase space; therefore, we used this radius to calculate ϕ of all other samples from the measured volume per particle.
21. A. van Blaaderen, P. Wiltzius, *Science* **270**, 1177 (1995).
22. E. R. Weeks, J. C. Crocker, A. C. Levitt, A. Schofield, D. A. Weitz, *Science* **287**, 627 (2000).
23. J. C. Crocker, D. G. Grier, *J. Colloid Interface Sci.* **179**, 298 (1996).
24. P. J. Steinhart, D. R. Nelson, M. Ronchetti, *Phys. Rev. B* **28**, 784 (1983).
25. The normalized order parameter $\hat{q}_l(i)$ of particle i has $(2l + 1)$ complex components

$$\hat{q}_{lm}(i) = \frac{1}{NB(i)} \sum_{j=1}^{B(i)} Y_{lm}(\hat{r}_{ij})$$

where N is a normalization factor such that $\sum_m \hat{q}_{lm}(i) \hat{q}_{lm}^*(i) = 1$, $B(i)$ is the number of neighbors of particle i , \hat{r}_{ij} is the unit vector pointing from particle i to its j th neighbor, and Y_{lm} is a spherical harmonic function. Two particles are defined as neighbors if their separation is smaller than a cutoff value of $2.83a$, chosen to be close to the minimum between the first and second peaks of the pair correlation function $g(r)$ for our samples. The “bond” between two neighboring particles i and j is recognized as crystal-like if the complex inner product $\sum_m \hat{q}_{lm}(i) \hat{q}_{lm}^*(j)$ exceeds a threshold value of 0.5. As in other studies (5, 9), we used the $l = 6$ order parameter.

26. In this context, “bond” denotes the direction that connects a particle with one of its neighbors and not a bond in the chemical sense.
27. Whether a nucleus was fully visible or not was decided by looking for particles in the nucleus that were closer than $0.8a$ to an edge of the observed volume. Nuclei that did not meet this criterion were not used to determine the probabilities p_g and p_s . A typical measurement contained between 1500 and 2500 subcritical and critical nuclei that were fully visible and could be tracked for some time.
28. Larger nuclei were not observed as often as smaller ones, because they have a higher free energy and, consequently, do not form as often. Thus, the bin size on the average crystallite radius $\langle r \rangle$ axis of Fig. 2 is increased logarithmically, which also reflects the accuracy with which the critical size can be identified.
29. Nucleation density rates obtained with particles of different sizes can be compared when expressed in dimensionless form using the intrinsic length and time scales. For this comparison, $D_0/(2a)^{-5}$ is used as the unit of the nucleation rate density, where $D_0 \approx 0.085 \mu\text{m}^2 \text{s}^{-1}$ is the free-particle diffusion constant.

30. K. Schätzel, B. J. Ackerson, *Phys. Rev. E* **48**, 3766 (1993).
 31. J. L. Harland, W. van Meegen, *Phys. Rev. E* **55** 3054 (1997).
 32. R. Ohnesorge, H. Löwen, H. Wagner, *Phys. Rev. E* **50**, 4801 (1994).
 33. $q_l(i)$ is a second-order rotational invariant of the $(2l + 1)$ -component bond-order parameter $q_l(i)$ for particle i and is defined by

$$q_l(i) = \left[\frac{4\pi}{2l+1} \sum_{m=-l}^l |q_{lm}(i)|^2 \right]^{\frac{1}{2}}$$

$w_l(i)$ is a third-order rotational invariant defined by

$$w_l(i) = \sum_{\substack{m_1, m_2, m_3 \\ m_1 + m_2 + m_3 = 0}} \begin{pmatrix} l & l & l \\ m_1 & m_2 & m_3 \end{pmatrix} \times q_{lm_1}(i)q_{lm_2}(i)q_{lm_3}(i)$$

where $(\cdot\cdot\cdot)$ stands for a Wigner $3j$ symbol.

34. The histograms for fcc, bcc, and hcp order were obtained from computer-generated crystal data. Random fluctuations were added to the particle positions in such a way that the width of the first peak of $g(r)$ for the computer-generated data matched the experimental value. The bond-order histograms were then

calculated in the same way as for particle positions from a measurement. The liquid histogram was taken from observations shortly after shear melting, when the sample was in the liquid state.

35. D. W. Marr, A. P. Gast, *Phys. Rev. E* **47**, 1212 (1993).
 36. R. L. Davidchack, B. B. Laird, *Phys. Rev. Lett.* **85**, 4751 (2000).
 37. This work was supported by NSF (grant DMR-9971432) and NASA (grant NAG3-2284). U.G. also acknowledges support by the Swiss National Science Foundation.

20 December 2000; accepted 28 February 2001

Capturing a Photoexcited Molecular Structure Through Time-Domain X-ray Absorption Fine Structure

Lin X. Chen,^{1*} Wighard J. H. Jäger,¹ Guy Jennings,² David J. Gosztola,¹ Anneli Munkholm,^{1†} Jan P. Hessler¹

The determination of the structure of transient molecules, such as photoexcited states, in disordered media (such as in solution) usually requires methods with high temporal resolution. The transient molecular structure of a reaction intermediate produced by photoexcitation of NiTPP-L₂ (NiTPP, nickeltetraphenylporphyrin; L, piperidine) in solution was determined by x-ray absorption fine structure (XAFS) data obtained on a 14-nanosecond time scale from a third-generation synchrotron source. The XAFS measurements confirm that photoexcitation leads to the rapid removal of both axial ligands to produce a transient square-planar intermediate, NiTPP, with a lifetime of 28 nanoseconds. The transient structure of the photo-dissociated intermediate is nearly identical to that of the ground state NiTPP, suggesting that the intermediate adopts the same structure as the ground state in a noncoordinating solvent before it recombines with two ligands to form the more stable octahedrally coordinated NiTPP-L₂.

Photoexcited states of molecules are often studied with “pump-probe” methods, in which a short optical pulse excites the ground state, and a second probe pulse interrogates the excited state. For structural studies, substantial progress has been made in generating ultrashort x-ray pulses (1–4) that have been used to obtain time-resolved x-ray diffraction information with picosecond resolution (5–7). Because many light-driven processes occur in disordered media, techniques that do not rely on the long-range order of a system must be developed. The approach of laser pump/x-ray probe x-ray absorption fine structure (XAFS) was proposed earlier (8–10), and transient molecular structures, generated in light-induced processes, were captured without using the temporal resolution of the source (11–19).

Here we present time-domain laser pump/x-ray probe XAFS studies using x-ray pulses from a third-generation synchrotron source. (The experiments were conducted at a wiggler beamline at the Basic Energy Sciences Synchrotron Research Center at Argonne National Laboratory’s Advanced Photon Source.) Although the duration of the x-ray pulses (100 ps at full width at half-maximum) is too long to follow atomic displacements due to the photoexcitation, it is suitable for capturing intermediate structures with subnanosecond resolution. We are able to take “snapshots” of molecules when the population of the laser-generated transient species reaches a maximum; in this case, the species is a reaction intermediate with a 28-ns lifetime that results from the photodissociation of NiTPP-L₂ (NiTPP, nickeltetraphenylporphyrin; L, piperidine) in solution (Fig. 1A).

The photoinduced processes of hemelike porphyrin derivatives are examples of how, through electron transfer, the coordination geometry of a metal ion is altered by the electronic structure of its macrocycle ligands. These molecules can serve as models for oxygen transport,

and the photoinduced redox reactions. According to previous studies (20–22) in a weakly coordinating or noncoordinating solvent, the $3d^8$ electrons of the Ni(II) ion in the square planar geometry of NiTPP adopt a singlet spin state $^1(3d_{z^2})^2$, S_0 , whereas these electrons in the octahedral geometry of NiTPP-L₂ prefer the triplet spin state $^3(3d_{x^2-y^2}, 3d_{z^2})$, T_0 . This difference reflects the response of the $3d_{x^2-y^2}$ and $3d_{z^2}$ orbitals in the square planar and octahedral ligand fields. Starting with NiTPP-L₂, a laser pump pulse induces an electronic transition from the triplet ground state, T_0 , to an excited triplet state, T^* (Fig. 1B). This state decays and undergoes intersystem crossing to an excited singlet state, S^* . This excited state ejects two ligands L to produce the square planar geometry (20–22). If the solvent were noncoordinating or weakly coordinating, this reaction sequence would be completed. However, in a strongly coordinating solvent, S_0 is unstable and the system will return to T_0 , by recombining with two piperidine ligands to form an octahedrally coordinated NiTPP-L₂ (Fig. 1). The transient structures involved in this recombination are not known. A penta-coordinated NiTPP-L molecule could be involved in the recombination, the square planar NiTPP could return to T_0 via a concerted axial chelation with two piperidine molecules, or an intermediate square pyramidal NiTPP-L structure could be important. Because it is difficult to identify a unique optical absorption spectrum for each possible intermediate involved in photodissociation, transient optical absorption spectra of NiTPP in coordinating solvent alone are not sufficient to identify the intermediates.

The excited-state dynamics of NiTPP-L₂ have been studied by ultrafast optical transient absorption and Raman spectroscopy (20–25). The intersystem crossing from T^* to S^* and the subsequent dissociation to S_0 occur in less than a few hundred picoseconds (22). In a strongly coordinating solvent at room temperature, this state of NiTPP has a lifetime of 28 ns, because it must react with two piperidine molecules to reform NiTPP-L₂. We can therefore use x-ray pulses from a synchrotron source to determine the local structure of these intermediates and compare them with the structure of ground state NiTPP. In addition, it is possible to determine whether an intermediate species with only one axial ligand is present (22). The experiment was

¹Chemistry Division and ²Materials Science Division, Argonne National Laboratory, Argonne, IL 60439, USA.

*To whom correspondence should be addressed. E-mail: lchen@anl.gov

†Present address: LumiLeds Lighting, 370 West Trimble Road, San Jose, CA 95131, USA.